

# Selective and Sensitive Photon Sieve Based on III–V Semiconductor Nanowire Forest Fabricated by Lithography-Free Process

Gil Ju Lee, Kwangwook Park, Min Seok Kim, Sehui Chang, Tae Joon Seok, Hong-Gyu Park, Gunwu Ju, Kyujung Kim, and Young Min Song\*

Vertically oriented semiconductor nanowires (NWs) have been intensely studied in macroscopic perspective due to their attractive applications such as optical filters, photodiodes, and solar cells. However, microscopic photonic phenomena of dense and random NWs have been rarely, and their promising applications have not been explored. Therefore, this article theoretically and experimentally investigates the microscopic photonic event of dense and random NWs using highly selective and sensitive photon sieve (SSPS), which employs highly populated III/V semiconductor NW forests fabricated with a lithography-free self-catalyzed growth method. Theoretical analyses reveal that diameter-dependent and selective photon absorption occurs even for a dense and disordered NW distribution. The engineered growth process affords highly populated NW forests (mean shortest interval = 192.4 nm) comprising NWs with a high aspect ratio (mean aspect ratio = 34.3) and a sufficiently broad diameter distribution to span the visible spectrum and decompose it (mean diameter = 94 nm, standard deviation = 49 nm). Moreover, the SSPS exhibits unique spectral responses to monochromatic light of different wavelengths (correlation coefficients < 0.03) and a high sensitivity with a highest absorptivity of 92.4%. This work indicates SSPSs can be utilized for various applications of artificial photoreceptor, physically unclonable function, and high efficient optoelectronics.

and high scattering,<sup>[8,9]</sup> which are utilized in the field of optoelectronics. As one of the candidates for refractive index modulation, vertically oriented semiconductor nanowires (NWs) are promising because of i) their high refractive index and extinction coefficient that cause strong light–matter interactions,<sup>[10,11]</sup> ii) diverse functionalities (e.g., wavelength selectivity or broadband absorption) depending on structural parameters including period and diameter,<sup>[12–16]</sup> iii) mechanical softness intrinsic to one-dimensional nanoscale structures,<sup>[17–19]</sup> and iv) inherent material advantages such as stability,<sup>[20,21]</sup> controllable electrical properties,<sup>[22–25]</sup> biocompatibility,<sup>[26,27]</sup> and mature fabrication/synthesis technologies.<sup>[10,11,24,28,29]</sup>

With these advantages, semiconductor NWs have provided route to advanced energy harvesting devices using tapered/multi-diameters III/V nanowire arrays,<sup>[12,30]</sup> core-shell Si nanowire arrays,<sup>[31,32]</sup> artificial photosynthesis for water splitting.<sup>[33]</sup> Moreover, high efficiency photodetectors by various vertical compound semiconductor NWs were

devised in ultraviolet (UV) range<sup>[34]</sup> and visible-to-near-infrared (NIR) range<sup>[35]</sup> and even in thermal wave range.<sup>[36,37]</sup> Besides these active optical devices, the geometrically induced optical resonances of vertical NWs have contributed to the development of optical filters with high selectivity for multi-band imaging,<sup>[38,39]</sup> high purity/changeable color filters,<sup>[13,18,40]</sup> and

## 1. Introduction

Light management is of paramount importance in numerous fields of science and technology. Photonic structures at the nano-/micro-scale are a powerful tool for manipulating light-matter interaction, such as anti-reflection,<sup>[1–4]</sup> perfect absorption,<sup>[5–7]</sup>

G. J. Lee, M. S. Kim, S. Chang, Prof. T. J. Seok, Prof. Y. M. Song  
School of Electrical Engineering and Computer Science (EECS)  
Gwangju Institute of Science and Technology (GIST)  
Gwangju 61005, Republic of Korea  
E-mail: ymsong@gist.ac.kr

Prof. K. Park  
Division of Advanced Materials Engineering  
Chonbuk National University  
Jeonju 54896, Republic of Korea

 The ORCID identification number(s) for the author(s) of this article can be found under <https://doi.org/10.1002/adom.202000198>.

Prof. H.-G. Park  
Department of Physics  
Korea University  
Seoul 02841, Republic of Korea

Dr. G. Ju  
Technology Support Center  
Korea Institute of Science and Technology  
Seoul 02792, Republic of Korea

Prof. K. Kim  
Department of Cogno-Mechatronics Engineering  
Pusan National University (PNU)  
Busan 46241, Republic of Korea

DOI: 10.1002/adom.202000198

optical anti-counterfeiting sticker.<sup>[15]</sup> However, these researches have focused on the collective optical feature of NWs and device performance, which could be observed and manifested in macroscopic scale. Although the individual resonance of combined NWs triggers the macroscopic observable optical characteristics, the detailed photonic phenomena in NW arrays have been barely studied so far.

Here, we present theoretical and experimental studies on microscopic optical behavior of highly dense and randomly distributed NW arrays embedded in a transparent polymer, which is called selective and sensitive photon sieve (SSPS) in our study. The proposed SSPS exhibits excellent wavelength selectivity, which can distinguish four wavelengths corresponding to red, green, blue, and NIR lights and high sensitivity corresponding to a maximum absorptivity of 92.4%. First, we computationally ascertained the feasibility of using randomized and dense NWs (i.e., a NW forest) for selective and sensitive wavelength absorption from the UV to visible or NIR depending on the NW diameters. Next, we fabricated the NW forest using a lithography-free/self-catalyzed gallium arsenide (GaAs) growth method on a (111) Si wafer, which is a cost-efficient fabrication method. To produce the SSPS, we isolated the nanowire

forest from the Si substrate by embedding the forest into a transparent polymer and exfoliating it with a razor blade after growth. Furthermore, we reconstructed a three-dimensional (3D) simulation model from the statistical data obtained from the optimum SSPS and visualized the 3D absorption profiles according to the incident wavelengths. Finally, we experimentally demonstrated the wavelength selectivity and sensitivity of the SSPSs by measuring their spectrally distinct image patterns and optical efficiencies.

## 2. Design Rules for Selective/Sensitive Photon Sieve (SSPS)

The vertically oriented semiconductor nanowires selectively capture the incident photons depending on their respective diameters (Figure 1a). The diameter-dependent optical resonance, which is well known as HE<sub>11</sub> mode coupling with the incident light,<sup>[10,13,41]</sup> facilitates spectrally selective absorption. For high sensitivity, GaAs was selected as the NW material since it has a high refractive index and extinction coefficient that enables strong light-matter interaction and absorption to

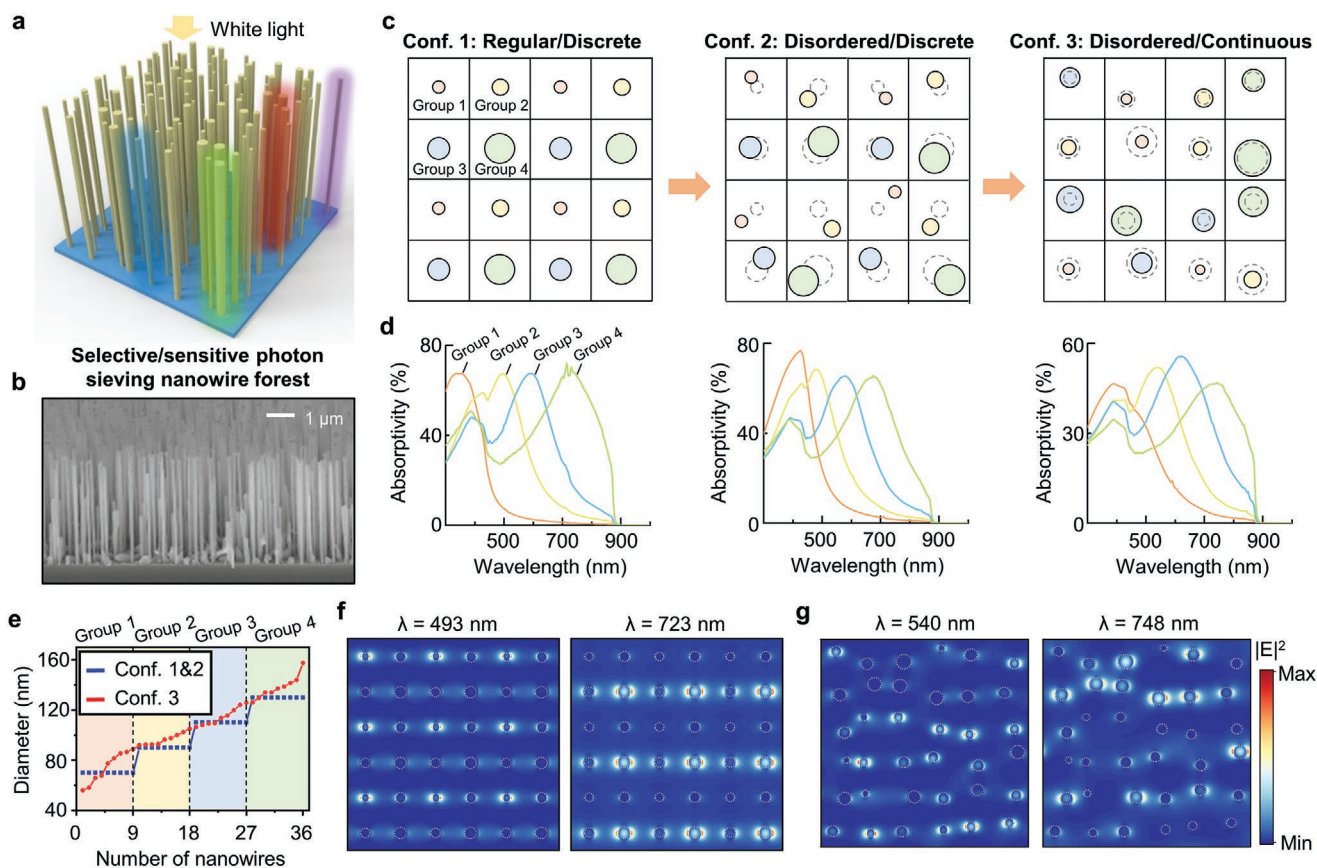


**Figure 1.** a) Schematic illustration of a selective and sensitive photon sieve based on a NW forest that exhibits diameter-dependent guided mode coupling with incident light. b) Tilt SEM image of the obtained NW forest on a Si substrate. c) Three configurations for diameter-dependent selective and sensitive photon absorption: i) Regular arrangement and discrete diameters, ii) disordered arrangement and discrete diameters, and iii) disordered arrangement and continuous diameters. NW diameters are classified into four groups indicated by different colors. d) Calculated absorption efficiency spectra of each group for each of the three configurations. e) Diameter distributions of the three configurations. Configurations 1 and 2 have discrete diameters of 70, 90, 110 and 130 nm, whereas Configuration 3 has continuous diameters ranging from 56 to 157 nm. f, g) Simulated electric field intensities of two configurations: (f) Configuration 1 at wavelengths of 493 nm and 723 nm and (g) Configuration 3 at wavelengths of 540 nm and 748 nm.

cover a wide wavelength range from UV to NIR (300–850 nm) (Figure S1). The scanning electron microscopy (SEM) image (Figure 1b) of the obtained NW forest exhibits a highly populated array with a high aspect ratio of  $\approx 34$ . Figure 1c shows schematics of the three configurations for selective photon absorption, which are a regular arrangement with four discrete diameters (Conf. 1: Regular/Discrete), disordered arrangement with four discrete diameters (Conf. 2: Disordered/Discrete), and disordered arrangement with continuous diameters corresponding to a random structure (Conf. 3: Disordered/Continuous). The NWs are grouped depending on the diameter, and each group shows wavelength selectivity, as shown in Figure 1d. In particular, despite the random arrangement and continuous diameters (Configuration 3), the NW forest shows selective and sensitive light absorption in the visible-NIR range.

In the simulations, SSPSs were isolated from the Si substrate to consider only the optical characteristics of the SSPSs. In the simulation model, the average interval between each nanowire is 350 nm and the nanowire height is 3  $\mu\text{m}$ . The

isolation procedure is shown in Figure S2 and described in **Methods**. In Configuration 1 and 2, the diameters are taken as 70, 90, 110, and 130 nm, whereas in Configuration 3, a Gaussian distribution with a mean of 100 nm and a standard variation of 20 nm was employed for diameter variation to represent the random structures (Figure 1e). The detailed simulation domains are shown in Figure S3. In addition, electric fields were calculated for Configuration 1 and 3 at the shortest and longest coupling wavelengths of 493 nm and 723 nm, and 540 nm and 748 nm, respectively (Figure 1f and g). These results demonstrate the diameter-dependent selective optical resonance.

**Figure 2a** shows the total absorption of SSPSs at the wavelength of 550 nm with different NW densities ( $\rho = 5, 10,$  and 20%) corresponding to NW counts (NW number = 20, 48, and 89). In the cases of  $\rho = 5$  and 10%, strongly absorbing NWs within a certain range of diameters are represented as red-to-white colors in the color scale, thus these active NWs control light absorption at the 550 nm-wavelength (i.e., selective absorption). However, the SSPS with  $\rho = 20\%$  shows weak absorptions

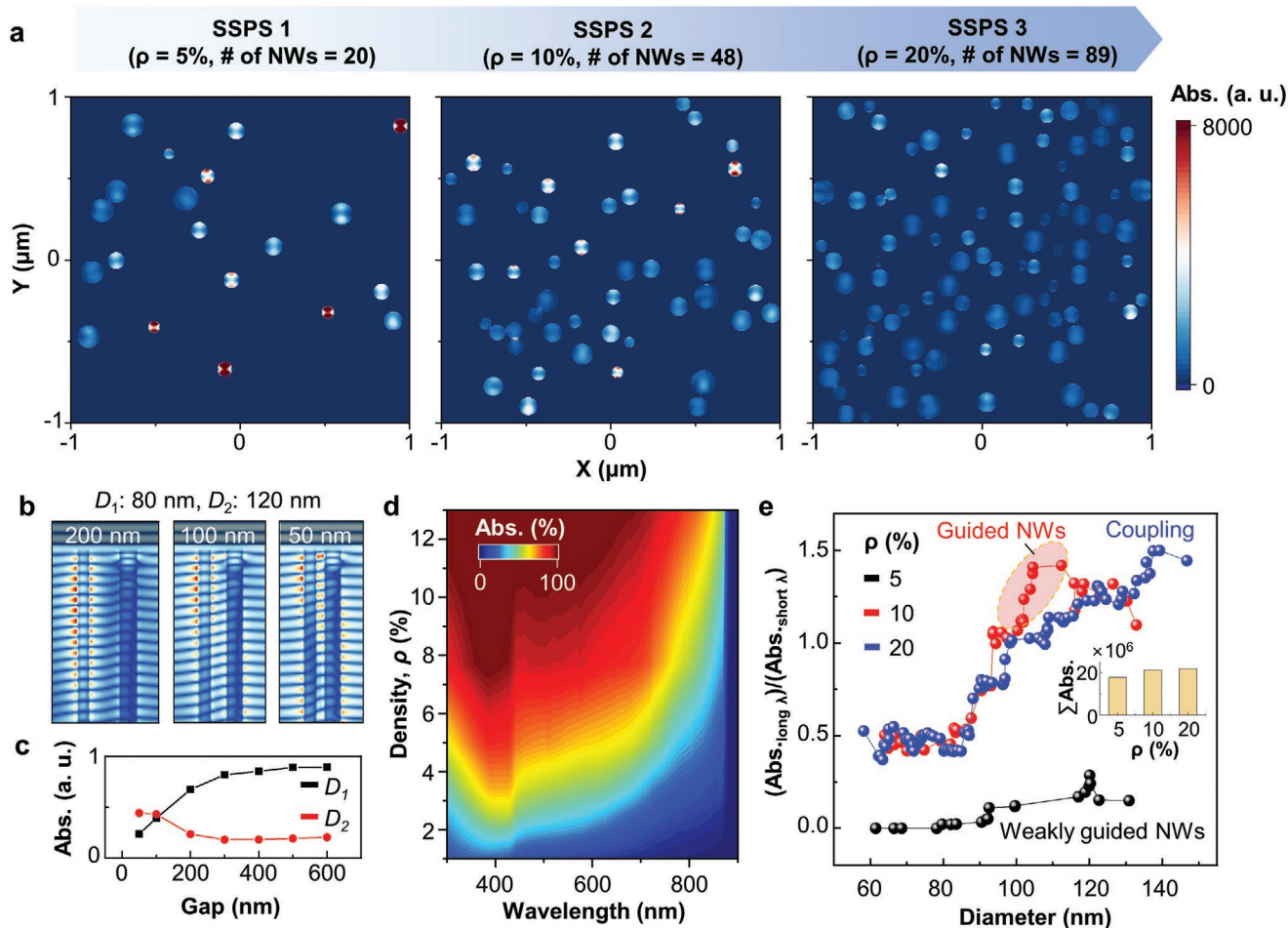


**Figure 2.** a) Simulated total absorption profiles of three SSPSs with different densities (i.e., 5, 10, and 20%) and numbers of NWs (NWs; i.e., 20, 48, and 89) at a wavelength of 550 nm. The absorption profiles represent the total absorption occurring in the NWs. b) Electric field simulations of two NWs with diameters of 80 and 120 nm (i.e.,  $D_1 = 80 \text{ nm}$  and  $D_2 = 120 \text{ nm}$ ) for three gap width of 200, 100, and 50 nm at a wavelength of 550 nm. c) Sum of absorption in two NWs as a function of gap width at a wavelength of 550 nm. For the small gap, guided mode coupling occurs in the adjacent NW. d) Contour map of SSPS absorption as a function of wavelength and density. e) Absorption ratios of three SSPSs at long and short wavelengths of 650 and 550 nm as a function of NW diameter. The inset shows the overall SSPS absorption at a wavelength of 550 nm.

in most NWs represented as blue colors. These results show that the SSPS with too high a density loses the selective absorption feature. Electric field simulations for two NWs with small and large diameters (i.e.,  $D_1 = 80$  nm and  $D_2 = 120$  nm) show that the guided mode is coupled from the small NW to the large NW as the gap between the two NWs decreases (Figure 2b). Thus, the light absorption in the NWs with a guided mode is coupled to the NWs without guided modes (Figure 2c). In the SSPS with  $\rho = 20\%$ , such a mode coupling between NWs leads to unselective absorption behavior.

Although the SSPS with low density,  $\rho = 5\%$ , displays a strong selective absorption behavior, it has a drawback in term of sensitivity (i.e., absorptivity) at longer wavelengths (Figure 2d). Therefore, a trade-off in density is required to achieve both selective and sensitive light absorption. Figure 2e summarizes the absorption behavior of three SSPSs as a function of NW diameter by comparing the absorption ratio between short and long wavelengths (i.e., 550 and 650 nm). The weak absorption of the low density SSPS (i.e.,  $\rho = 5\%$ ) at longer wavelengths results in a very low absorption ratio for all diameters. Also, in the dense SSPS (i.e.,  $\rho = 20\%$ ), a strong absorption by the

guided mode NWs is not found due to the mode coupling, but merely an increase in absorption is observed owing to the larger cross-sectional area at larger diameter. However, the SSPS with  $\rho = 10\%$  presents a strong absorption in the diameter range 100–115 nm, which is responsible for selective absorption at the 550 nm-wavelength. These theoretical analyses reveal that the proper density of the SSPS is  $\approx 10\%$ .

### 3. Fabrication of SSPS and Structural Parameter Analyses

Usually, NWs are fabricated using nanolithography processes,<sup>[42,43]</sup> which are prohibitively expensive for large-area manufacturing. In our study, the oriented GaAs NWs were grown on a semi-insulating (111) Si substrate by a lithography-free self-catalyzed growth method, reducing the production cost considerably (Figure S4 and Methods). Furthermore, unlike Au-catalyzed NWs, the self-catalyzed NWs do not require Au as a catalyst, thus eliminating the non-radiative recombination centers resulting from Au diffusion.<sup>[44]</sup> Figure 3a summarizes

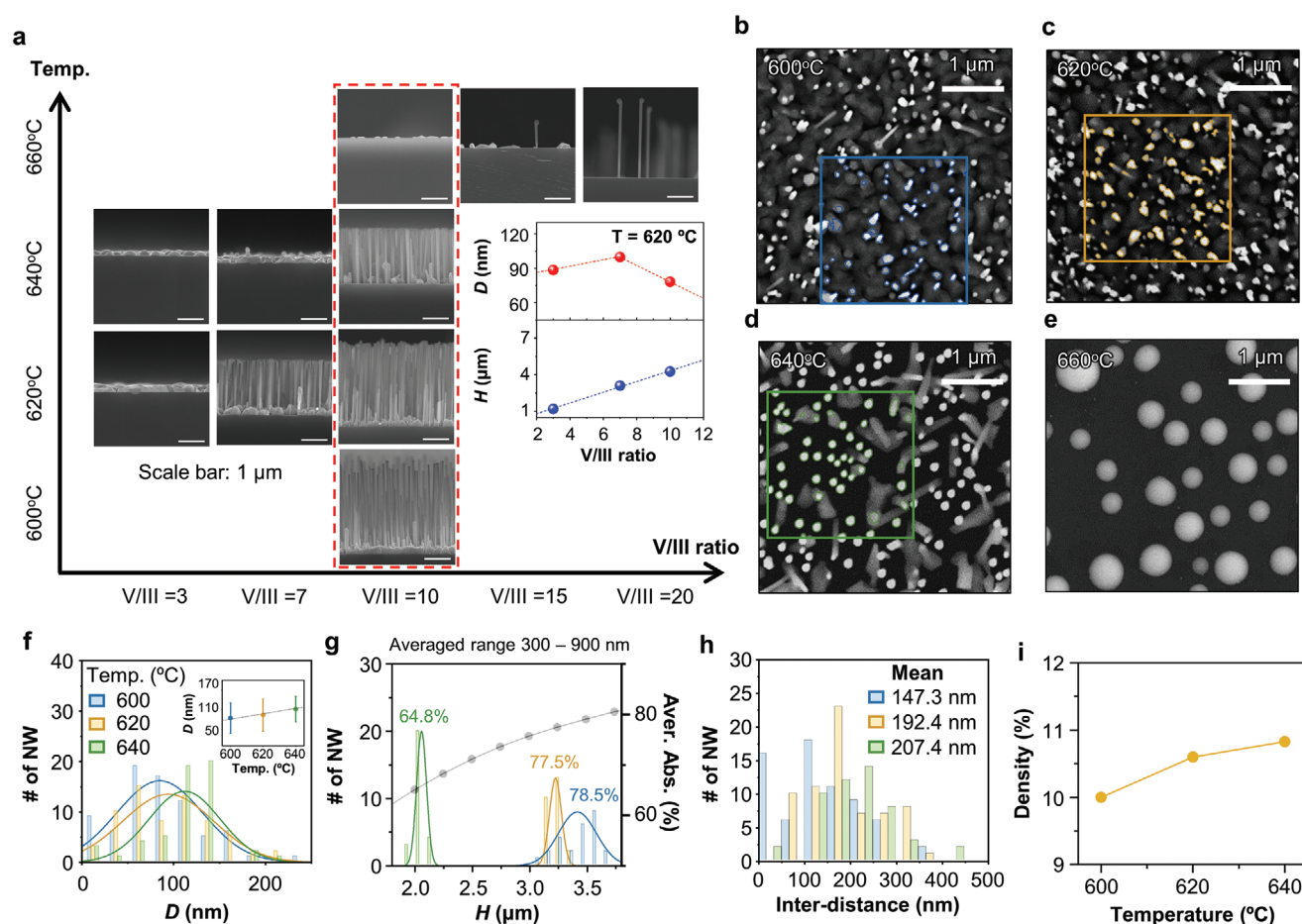


**Figure 3.** a) Cross-sectional view of GaAs NWs grown by changing the two growth parameters of V/III ratio and temperature, resulting in three different structures of NWs, clusters, and droplets. The inset graph shows the height and diameter of GaAs NWs as a function of V/III ratio at 620 °C. b–e) Plan views of the NWs with a V/III ratio of 10 enclosed in the red box in (a). The sample grown at 660 °C does not show any GaAs NWs. The blue, orange, and green boxes in (b–d) indicate the simulation domains of 3D modeling presented in Figure 4. f–i) Statistical analysis of geometric parameters of grown GaAs NWs for three growth temperatures: (f) diameter distribution, (g) height distribution, (h) shortest interval between NWs, and (i) density.

the growth process of GaAs NWs grown using various V/III ratios and growth temperatures. The minimum growth temperature for a successful NW growth increases with increasing V/III ratio. Furthermore, with a decrease in V/III ratio, the NW length decreased due to the lack of a molecular beam supply. On the other hand, the NW density drastically decreased at a high V/III ratio due to the increase in minimum growth temperature and the excessive desorption of impinging atoms. Hence, a V/III ratio of 10 was selected as the optimum growth condition.

Figure 3b–e show plan views of the NWs grown at different growth temperatures in the range of 600–660 °C at a V/III ratio of 10. It is noteworthy that the sample grown at 660 °C does not show any NWs but only droplet-like structures on the substrate. This is due to the decomposition of NWs by excessive surface adatom diffusion at the high substrate temperature.<sup>[45]</sup> On the other hand, when the growth temperature is too low, there are no NWs but only a polycrystalline GaAs layer due to the inhibition of surface adatom diffusion. This result indicates that the optimum growth temperature is in the range of 620–640 °C. This temperature range is consistent with a previously reported result.<sup>[46]</sup> In addition to the growth parameters (i.e., temperature and V/III ratio), the surface status of Si substrate during NW growth is a key parameter in the self-catalyzing growth process. To generate a proper condition of the surface, a controlled native oxide on the silicon substrate is required (Figure S5). With the appropriate surface treatment and growth conditions, the NW geometry can be reliably reproduced (Figure S6).

Figure 3f–i present detailed statistical analyses of the sample areas marked with blue, orange, and green boxes in Figure 3b–d. The NWs grown at 620 °C exhibit the greatest variation in diameter from 50 nm to 145 nm with an average diameter of approximately 94 nm (Figure 3f). The statistical analysis of the NW diameter shows that the average diameters increased from 80 nm to 110 nm with an increase in growth temperature (inset of Figure 3f). Unlike the radial growth of NWs, the axial growth is suppressed at a higher growth temperature due to the thermal desorption of impinging atoms (Figure 3g).<sup>[47]</sup> To estimate the height-dependence of absorption, the average absorption efficiencies were calculated using the pseudo-random structures described in Figure S7. At a growth temperature of 640 °C, 2- $\mu$ m-long NWs were grown, with a significantly low absorption efficiency of 64.8%. On the other hand, the NWs grown at growth temperatures of 620 and 600 °C exhibited improved average absorption efficiencies of  $\approx$ 78%.

Furthermore, the shortest inter-distances between the NWs were analyzed for all the samples (Figure 3h), which showed that the higher the temperature the longer is the distance between the NWs (1473, 192.4, and 2074 nm for 600, 620, and 640 °C, respectively). Based on the above computational study, the NWs should have a distance over 100 nm between each other to prevent the guided mode transition. Hence, the degradation of selective absorption is not expected because the aforementioned shortest inter-distance is sufficient for all the grown NW forests. Moreover, as shown in Figure 3i, the NWs grown at 620 and 640 °C exhibited a high density of over 10.5%, which is defined as the ratio of the NW area to the selected box area ( $2.364 \times 2.364 \mu\text{m}^2$ ), as observed from the plan SEM images.

The densities of NWs obtained under the three growth conditions are sufficient to enhance the light-sensitivity of the NW forest as shown in the above theoretical analyses.

#### 4. Computational Modeling of the Fabricated SSPS

To examine the selective absorption of the fabricated SSPS at 620 °C, a 3D simulation model (Figure S8) was produced using the SEM images and statistics shown in Figure 2c. The theoretical analyses confirm the wavelength selectivity of the SSPSs (Figure 4). The simulated wavelengths are 455, 555, 650, and 800 nm. The diameter-dependent electromagnetic resonance of the SSPS indicates that the groups of NWs responding to incident light are distinct and depend on the optical wavelength. Such a response of the NWs according to the wavelength of the incident light is represented as the spatially different absorption distribution within the NW arrays. As can be seen in the 3D absorption profiles, small-diameter NWs absorb when short-wavelength light is incident, whereas large-diameter NWs respond to long-wavelength light (magnified insets of Figure 4a). At a short wavelength, such as 455 nm, the majority of NWs strongly absorbing the incident light have small diameters, whereas a strong absorption of longer wavelengths is observed for NWs having larger diameters. The orange dashed boxes show strongly absorbing NWs at each wavelength. The absorption distributions of the NWs are distinguishable under incident light of different wavelengths (Figure 4b). These results demonstrate that the SSPS can respond to incident light differently, both spectrally and spatially, with a high sensitivity.

#### 5. Experimental Demonstration of Optical features of the SSPS

To experimentally examine the wavelength selectivity of the SSPS, the six fabricated samples were characterized by optical microscopy by illuminating them with white light and detecting optically filtered light at the wavelengths of 450, 550, 632.8, and 750 nm (Figure 5a, see Figure S9 for the spectra of the filter and measurement setup). Figure 5b shows micrographs of the responses of the SSPS under illumination of 450, 550, 632.8, and 750 nm. Under this monochromatic illumination, different spectral responses were obtained. The spectral response to 450 nm-wavelength shows the largest dark area compared to other images. This can be explained by the absorption in small and large diameter NWs. Obviously, small diameter NWs strongly absorb the short wavelength, but NWs with large diameters consume that wavelength shown in Figure 4b. The reconstructed response (RR), reconstructed from the R, G, B responses, is remarkably similar to the white light response (WLR) (Figure 5c). Also, the 2D correlation coefficients ( $\approx$ 0.75) between the WLR and RR illustrate that these two responses are almost indistinguishable for all six samples. The responses of all the SSPSs are shown in Figure S10.

Also, the 2D correlation coefficients were continuously used to evaluate the spatial correlation of the monochromatic images by comparing the binarized spectral image patterns (Figure 5e). The 2D correlation coefficients of the six pairs of spectral image

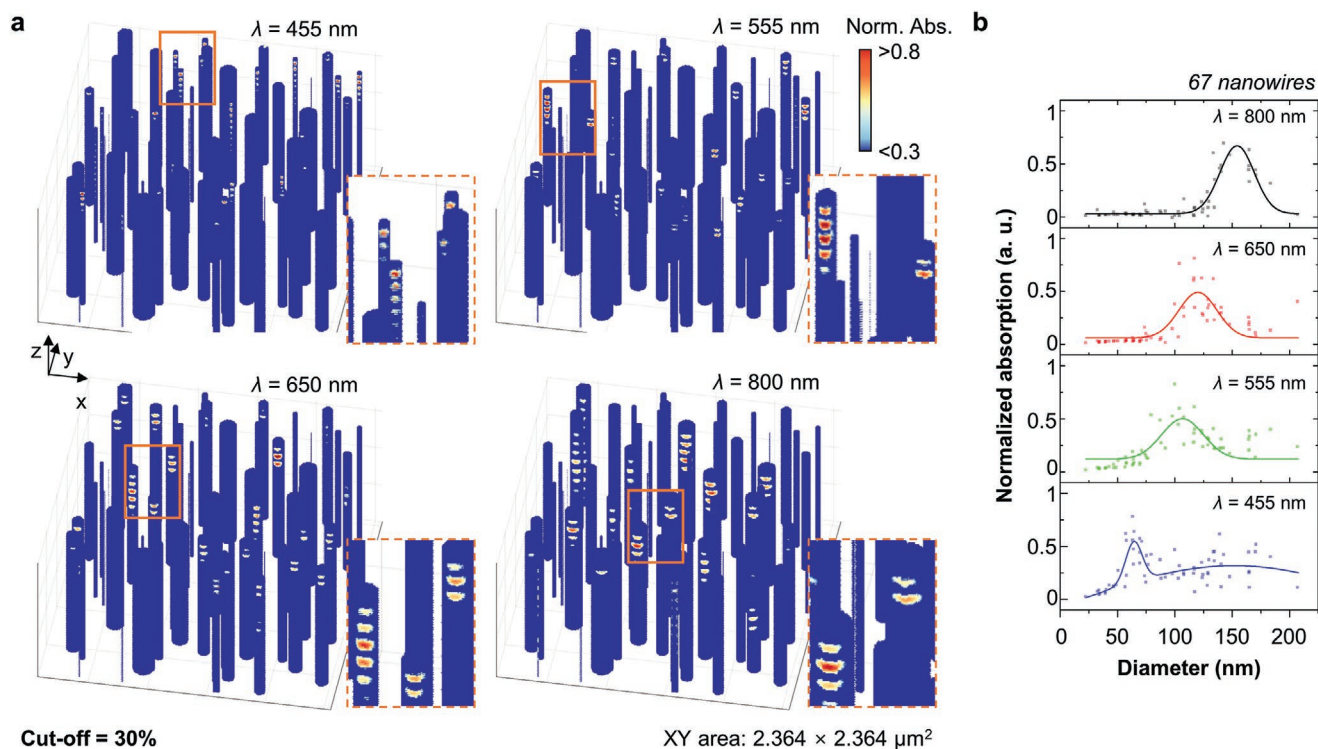


**Figure 4.** a) Simulated 3D absorption profiles of the representative SSPS at wavelengths of 455, 555, 650, and 800 nm, for a growth temperature of 620 °C and III/V ratio of 10. The absorption under 0.3 is cut-off to increase visibility. The insets show magnified images of the highly absorbing NWs at each wavelength. b) Diameter distributions of NWs absorbing at each incident wavelength in Figure 3d. The number of NWs in the region is 67. The solid lines indicate the fitted curves.

patterns show negligible correlations between each other and correspond to 2D correlation coefficients of less than 0.03 (Figure 5f). These results exhibit the set of NWs that absorb at each wavelength are totally different in each wavelengths. Although the abovementioned theoretical analyses shown in Figure 4 show that the partial overlap between the set of NWs exists, the patterns of reacted NWs are unique.

To investigate the sensitivity of the SSPS, the optical efficiencies including reflectance, transmittance, and absorptivity of the SSPS were obtained for filtered light of three colors (Figure 5g). The detailed optical efficiency measurement method is described in Methods. The waveguide-based coupling of the NW forest leads to high absorptivities of 92.4, 88.4, 80.3, and 64.0% corresponding to blue, green, red, and NIR light, respectively. The experimental results demonstrate that the SSPS based on GaAs NW forests have wavelength selectivity and high sensitivity in the visible and NIR range.

## 6. Conclusions

We presented a fabrication approach for a selective and sensitive photon sieve (SSPS) using disordered GaAs NW forests grown by a lithography-free process. Theoretical analyses revealed that spectrally selective absorption occurs even for random NW structures having continuous diameter distributions and disordered NW intervals. Based on the theoretical

analyses, we grew dense GaAs NW forests on a Si substrate with high-aspect ratio NWs by using a lithography-free self-catalyzed growth process. In addition, we analyzed and optimized the growth conditions of temperature and III/V ratio to control the geometrical parameters of the NWs such as height, diameter, shortest nanowire-to-nanowire interval, and density. In addition, the reproducibility of the self-catalyzed GaAs NW growth was ensured. After growing NW forests, we detached them from the Si substrate using a transparent polymer and a razor blade. To investigate the absorption phenomena in the SSPS, full-wave optical simulations were performed for a 3D model of the SSPS generated from SEM images and statistical analysis results. Theoretical analyses of the spatial absorption showed that groups of SSPS NWs responded differently depending on the incident wavelength. The spectral responses of the SSPS to red, green, blue, and NIR light, as obtained by optical microscopy, revealed negligible correlations between each other, under 0.03; this clearly indicated that the NWs in the SSPS respond differently to different colored incident light. Furthermore, the remarkably strong absorptivities for each wavelength showed the high sensitivity of the SSPS toward light with different spectra. Collectively, these features can also address some of the greatest challenges in optoelectronics such as the production of sensitive, selective, and conformal components for photodetectors and photovoltaics. Also, this successful demonstration can provide a new pathway to self-powered artificial photoreceptors<sup>[48–50]</sup> and optical physically unclonable function with high encoding capacity.<sup>[51,52]</sup>

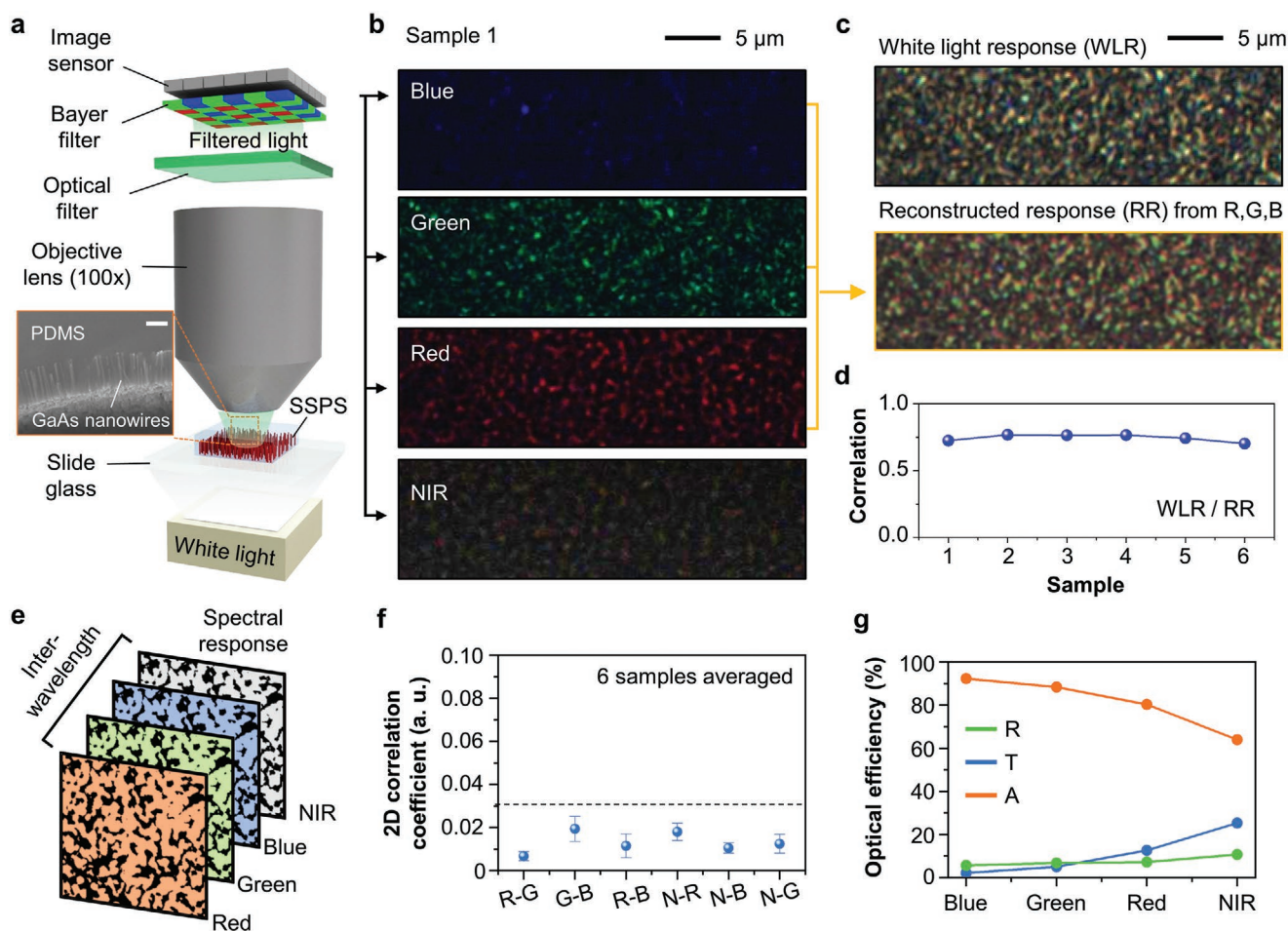


**Figure 5.** a) Schematic illustration of measurement setup to observe the selective absorption feature of the SSPS. The inset shows a cross-sectional SEM image of the SSPS. b) Optical microscope images of SSPS through optical filters: 450 nm filtered light, 550 nm filtered light, 632.8 nm filtered light, and 750 nm filtered light. All images are of the same region of the SSPS. c) Images of (top) white light response (WLR), and reconstructed response (RR) from red, green, and blue micrographs. d) 2D correlation coefficients of WLR and RR for six samples. e) Schematic of inter-wavelength 2D correlation. The letters of R, G, B, and N indicate red, green, blue, and NIR, respectively. f) 2D correlation coefficients of each filtered image of the six samples. g) Measured optical efficiencies of reflectance (R), transmittance (T), and absorptivity (A) at the center wavelengths of the filtered incident light (i.e., 450, 550, 632.8, and 750 nm).

## 7. Experimental Section

**Numerical Simulation:** To obtain spectral results, full-field 3D simulations were performed using the commercial electromagnetic software package (DiffractMOD, RSoft; USA) based on the rigorous coupled wave analysis (RCWA) method. To simplify all simulations, infinite periodicity was rendered for normal incidence. For the calculations, a grid size of  $0.1 \text{ nm}^2$  and thirteen diffraction orders were used to calculate the optical efficiencies, which were sufficient for numerical stability of the results. In electric field simulations, a 3D finite-difference time-domain (FDTD) method, which is built into DiffractMOD, was used. The same grid size was utilized in the simulation of electric field distributions. To obtain 3D absorption profiles, the FDTD method was used, and a volume monitor that has the same dimension as that of the simulation domain was exploited to observe the absorption in the NWs. After calculation, MATLAB (Mathworks, USA) was used to obtain 3D absorption profiles of the SSPS. Material dispersion and extinction coefficients of GaAs were also considered in order to obtain accurate calculation results. The complex refractive indices of GaAs were obtained by ellipsometric measurement (Figure S1). A refractive index of 1.43 was used for polydimethylsiloxane (PDMS).<sup>[39]</sup>

**Growth of GaAs Nanowire Forest:** The samples used in this study were grown on semi-insulating (111) Si substrates using a molecular beam epitaxy (MBE) system equipped with a valved cracker effusion cell ( $\text{As}_4$ ) source. For group-III elemental sources, conventional K-cells with linear motion shutters were employed. The growth temperature was measured using an infrared pyrometer (IRCON Modline 3G) having a measurement range of 350–1400 °C with a measurement accuracy of  $\pm 0.6\%$ . Prior to sample growth, the substrate native oxide was removed by buffered oxide etch (BOE), and the substrates were kept in a dry air atmosphere for a week to form a controlled native oxide having the same physical properties to rule out its effect on NW growth. This substrate (with controlled native oxide) was then loaded into a growth chamber and annealed for 30 min at 770 °C. GaAs NWs were grown by a self-catalyzing technique by exposing the substrate surfaces to a Ga molecular beam flux for 2 min at each growth temperature (600, 620, 640, and 660 °C). The estimated growth rate of Ga was  $0.145 \text{ nm/s}$ , which was obtained by reflection high-energy electron diffraction (RHEED) during Ga deposition. Immediately after leaving the substrate for 30 s in the absence of any molecular beam flux to stabilize the Ga droplets, GaAs NWs were grown by opening the As valve and Ga shutter simultaneously for 30 min while keeping the V/III ratio at around 10. The

beam equivalent pressure (BEP) of As was  $3.2 \times 10^6$  Torr in the form of the tetramer ( $As_4$ ) instead of the dimer ( $As_2$ ) to allow Ga to have a long diffusion length at the growth front.<sup>[53]</sup> Throughout the growth process, the substrate was rotated at 7 rpm. When sample growth was complete, both the Ga shutter and As valve were closed and the substrate was cooled to 200 °C. The entire growth procedure is illustrated in Figure S4.

**Fabrication of SSPS by Embedding a Transparent Polymer:** The process of transferring the grown NWs from the Si substrate to a transparent polymer is crucial to fabricating the SSPS. PDMS, which exhibits near-zero absorption in the visible and near-infrared regions, was used as the transparent polymer. Figure S2 shows the fabrication method for the SSPS.<sup>[39]</sup> The PDMS mixed with a base and curing agent in the ratio of 5:1 was spin-coated at 1000 rpm for 60 s onto the prepared GaAs NWs. The coated PDMS layer was cured at 230 °C on a hot plate for 1 h. The cured PDMS thickness was over 40 μm, which exceeds the height of the NWs. The cured PDMS film in which the NWs were embedded was detached by scraping it away from the substrate with a razor blade, according to a reported method. The SEM image of the interface between the PDMS film and Si substrate shows that only a little of the bottom of the NWs remains on the Si substrate, while the rest of the NWs are transferred to the PDMS intact (Figure S2).

**Characterization:** The optical characteristics of transmittance, reflectance, and absorptivity were measured using an UV–vis–near-infrared spectrophotometer (Cary 5000 UV-Vis-NIR, Agilent Technologies, USA) with an unpolarized light source. A scanning electron microscope (S-4700, Hitachi Hightechnology, Japan) was used to obtain the SEM images of the NW forests.

**Measurement of Spectral Response:** For optical microscopy measurements, we customized measurement setup composed of a white light source (MCWHL6, Thorlabs, Inc., Germany) with a collimated lens (SM2F32-B, Thorlabs, Inc., Germany), an aperture, an objective lens (MPlanFL N 100 ×/0.9NA BD objective, Olympus, Japan), a color filter rotator (CFW6, Thorlabs, Inc., Germany) with R,G,B, and NIR pass filters (FB450-10, FB550-10, FB632.8-10, FB750-10; Thorlabs, Inc., Germany), tube lens (KPX088, Newport, USA), and CMOS image sensor (Grasshopper G33-U3-23S6C-C, FLIR, USA). The white light source was operated by a DC power supply. The cover glass and IR filter in CMOS sensor were removed to capture the NIR light. For NIR light, a tungsten light bulb was used as the light source. Four different color filters with red, green, blue, and NIR transmission wavelengths were exploited to approximate monochromatic light. The spectra of each filter is shown in Figure S9a.

**Correlation Calculations of the Spectral Responses:** Commercial software (MATLAB, USA, Mathworks, Inc.) was used to calculate the 2D correlation coefficients. We computed the coefficients using Equation (1)<sup>[54]</sup>

$$r = \frac{\sum_m \sum_n (A_{mn} - \bar{A})(B_{mn} - \bar{B})}{\sqrt{(\sum_m \sum_n (A_{mn} - \bar{A})^2)(\sum_m \sum_n (B_{mn} - \bar{B})^2)}} \quad (1)$$

where  $A$  and  $B$  are two input arrays (i.e., spectral responses), and  $\bar{A}$  and  $\bar{B}$  are the averages of  $A$  and  $B$ . The subscripts,  $m$  and  $n$ , indicate the indices corresponding to the positions of the numeric elements in each input array.

## Supporting Information

Supporting Information is available from the Wiley Online Library or from the author.

## Acknowledgements

The authors G. J. Lee and K. Park contributed equally to this work. This research was supported by the National Research Foundation (NRF)

of Korea (NRF-2018R1A4A1025623, NRF-2017M3D1A1039288, NRF-2018M3D1A1058997) and by the Korea Institute of Energy Technology Evaluation and Planning (KETEP) and the Ministry of Trade, Industry & Energy (MOTIE) of the Republic of Korea (No. 20183010014310). G. J. Lee acknowledges support from the NRF (NRF-2017H1A2A1042138).

## Conflict of Interest

The authors declare no conflict of interest.

## Keywords

gallium arsenide, nanowire forest, selective and sensitive photon absorber, self-catalyzed growth

Received: February 4, 2020

Revised: May 27, 2020

Published online:

- [1] J. K. Song, D. Son, J. Kim, Y. J. Yoo, G. J. Lee, L. Wang, M. K. Choi, J. Yang, M. Lee, K. Do, J. H. Koo, N. Lu, J. H. Kim, T. Hyeon, Y. M. Song, D.-H. Kim, *Adv. Funct. Mater.* **2017**, *27*, 1605286.
- [2] Y. M. Song, H. J. Choi, J. S. Yu, Y. T. Lee, *Opt. Express* **2010**, *18*, 13063.
- [3] Y. M. Song, S. J. Jang, J. S. Yu, Y. T. Lee, *Small* **2010**, *6*, 984.
- [4] J. Cai, L. Qi, *Mater. Horiz.* **2015**, *2*, 37.
- [5] R. H. Siddique, Y. J. Donie, G. Gomard, S. Yalamanchili, T. Merdzhanova, U. Lemmer, H. Hölscher, *Sci. Adv.* **2017**, *3*, e1700232.
- [6] J. Gong, F. Yang, X. Zhang, *J. Phys. D: Appl. Phys.* **2017**, *50*, 455105.
- [7] H. Lin, B. C. P. Sturmberg, K.-T. Lin, Y. Yang, X. Zheng, T. K. Chong, M. D. Sterke, B. Jia, *Nat. Photonics* **2019**, *13*, 270.
- [8] S. H. Choi, S.-W. Kim, Z. Ku, M. A. Visbal-Onufrak, S.-R. Kim, K.-H. Choi, H. Ko, W. Choi, A. M. Urbas, T.-W. Goo, Y. L. Kim, *Nat. Commun.* **2018**, *9*, 452.
- [9] Y.-C. Chao, C.-Y. Chen, C.-A. Lin, J.-H. He, *Energy Environ. Sci.* **2011**, *4*, 3436.
- [10] P. J. Pauzauskie, P. Yang, *Mater. Today* **2006**, *9*, 36.
- [11] P. Yang, R. Yan, M. Fardy, *Nano Lett.* **2010**, *10*, 1529.
- [12] K. T. Fountaine, W.-H. Cheng, C. R. Bukowsky, H. A. Atwater, *ACS Photonics* **2016**, *3*, 1826.
- [13] K. Seo, M. Wober, P. Steinvurzel, E. Schonbrun, Y. Dan, T. Ellenbogen, K. B. Crozier, *Nano Lett.* **2011**, *11*, 1851.
- [14] K. T. Fountaine, W. S. Whitney, H. A. Atwater, *J. Appl. Phys.* **2014**, *116*, 153106.
- [15] H. S. Song, G. J. Lee, D. E. Yoo, Y. J. Kim, Y. J. Yoo, D.-W. Lee, V. Siva, I.-S. Kang, Y. M. Song, *Sci. Rep.* **2019**, *9*, 3350.
- [16] S. Kim, K.-H. Kim, D. J. Hill, H.-G. Park, J. F. Cahoon, *Nat. Commun.* **2018**, *9*, 2781.
- [17] S. Wang, Z. Shan, H. Huang, *Adv. Sci.* **2017**, *4*, 1600332.
- [18] Y. J. Kim, Y. J. Yoo, G. J. Lee, D. E. Yoo, D.-W. Lee, V. Siva, H. S. Song, I. S. Kang, Y. M. Song, *ACS Appl. Mater. Interfaces* **2019**, *11*, 11849.
- [19] Y. Wu, H. Yan, M. Huang, B. Messer, J. H. Song, P. Yang, *Chem. - Eur. J.* **2002**, *8*, 1260.
- [20] H. J. Joyce, J. L. Boland, C. L. Davies, S. A. Baig, M. B. Johnston, *Semicond. Sci. Technol.* **2016**, *31*, 103003.
- [21] T. J. Kempa, R. W. Day, S. K. Kim, H.-G. Park, C. M. Lieber, *Energy Environ. Sci.* **2013**, *6*, 719.
- [22] B. Tian, X. Zheng, T. J. Kempa, Y. Fang, N. Yu, G. Yu, J. Huang, C. M. Lieber, *Nature* **2007**, *449*, 885.
- [23] M. S. Gudiksen, L. J. Lauhon, J. Wang, D. C. Smith, C. M. Lieber, *Nature* **2002**, *415*, 617.

- [24] W. Y. Huynh, J. J. Dittmer, A. P. Alivisatos, *Science* **2002**, 295, 2425.
- [25] S. Gradečak, F. Qian, Y. Li, H.-G. Park, C. M. Lieber, *Appl. Phys. Lett.* **2005**, 87, 173111.
- [26] A. K. Shalek, J. T. Robinson, E. S. Karp, J. S. Lee, D.-R. Ahn, M.-H. Yoon, A. Sutton, M. Jorgolli, R. S. Gertner, T. S. Gujral, G. MacBeath, E. G. Yang, H. Park, *Proc. Natl. Acad. Sci. USA* **2010**, 107, 1870.
- [27] Y. Cui, Q. Wei, H. Park, C. M. Lieber, *Science* **2001**, 293, 1289.
- [28] D. V. Talapin, J. H. Nelson, E. V. Shevchenko, S. Aloni, B. Sadtler, A. P. Alivisatos, *Nano Lett.* **2007**, 7, 2951.
- [29] F. Qian, Y. Li, S. Gradečak, H.-G. Park, Y. Dong, Y. Ding, Z. L. Wang, C. M. Lieber, *Nat. Mater.* **2008**, 7, 701.
- [30] K. T. Fountaine, C. G. Kendall, H. A. Atwater, *Opt. Express* **2014**, 22, A930.
- [31] X. Wang, K. L. Pey, C. H. Yip, E. A. Fitzgerald, D. A. Antoniadis, *J. Appl. Phys.* **2010**, 108, 124303.
- [32] M. Adachi, M. Anantram, K. Karim, *Sci. Rep.* **2013**, 3, 1546.
- [33] F. A. Chowdhury, M. L. Trudeau, H. Guo, Z. Mi, *Nat. Commun.* **2018**, 9, 1707.
- [34] A. Bilgaiyan, T. Dixit, I. A. Palani, V. Singh, *Physica E* **2017**, 86, 136.
- [35] L. Zeng, S. Lin, Z. Lou, H. Yuan, H. Long, Y. Li, W. Lu, S. P. Lau, D. Wu, Y. H. Tsang, *NPG Asia Mater.* **2018**, 10, 352.
- [36] J. Svensson, N. Anttu, N. Vainorius, B. M. Borg, L.-E. Wernersson, *Nano Lett.* **2013**, 13, 1380.
- [37] C.-H. Kuo, J.-M. Wu, S.-J. Lin, W.-C. Chang, *Nanoscale Res. Lett.* **2013**, 8, 327.
- [38] G. J. Lee, Y. J. Kim, H. S. Song, D. E. Yoo, D.-W. Lee, I.-S. Kang, Y. M. Song, *Adv. Intell. Syst.* **2019**, 1, 1900072.
- [39] H. Park, K. Seo, K. B. Crozier, *Appl. Phys. Lett.* **2012**, 101, 193107.
- [40] Y. J. Kim, Y. J. Yoo, M. H. Kang, J. H. Ko, M. R. Park, D. E. Yoo, D. W. Lee, K. Kim, I.-S. Kang, Y. M. Song, *Nanophotonics* **2020**, 0, 20200062.
- [41] B. Wang, P. W. Leu, *Opt. Lett.* **2012**, 37, 3756.
- [42] C. Lin, M. L. Povinelli, *Opt. Express* **2011**, 19, A1148.
- [43] M.-C. Sun, G. Kim, J. H. Lee, H. Kim, S. W. Kim, H. W. Kim, J.-H. Lee, H. Shin, B.-G. Park, *Microelectron. Eng.* **2013**, 110, 141.
- [44] S. Breuer, C. Pfüller, T. Flissikowski, O. Brandt, H. T. Grah, L. Geelhaar, H. Riechert, *Nano Lett.* **2011**, 11, 1276.
- [45] S. Hertenberger, D. Rudolph, J. Becker, M. Bichler, J. J. Finley, G. Abstreiter, G. Koblmüller, *Nanotechnology* **2012**, 23, 235602.
- [46] F. Matteini, V. G. Dubrovskii, D. Ruffer, G. Tütüncüoğlu, Y. Fontana, A. F. Morral, *Nanotechnology* **2015**, 26, 105603.
- [47] S. Paiman, Q. Gao, H. J. Joyce, Y. Kim, H. H. Tan, C. Jagadish, X. Zhang, Y. Guo, J. Zou, *J. Phys. D: Appl. Phys.* **2010**, 43, 445402.
- [48] J. Tang, N. Qin, Y. Chong, Y. Diao, Yiliguma, Z. Wang, T. Xue, M. Jiang, J. Zhang, G. Zheng, *Nat. Commun.* **2018**, 9, 786.
- [49] K. Mathieson, J. Loudin, G. Goetz, P. Huie, L. Wang, T. I. Kamins, L. Galambos, R. Smith, J. S. Harris, A. Sher, D. Palanker, *Nat. Photonics* **2012**, 6, 391.
- [50] H. Lorach, G. Goetz, R. Smith, X. Lei, Y. Mandel, T. Kamins, K. Mathieson, P. Huie, J. Harris, A. Sher, D. Palanker, *Nat. Med.* **2015**, 21, 476.
- [51] M. R. Carro-Temboury, R. Arppe, T. Vosch, T. J. Sørensen, *Sci. Adv.* **2018**, 4, e1701384.
- [52] T. McGrath, I. E. Bagci, Z. M. Wang, U. Roedig, R. J. Young, *Appl. Phys. Rev.* **2019**, 6, 011303.
- [53] C. Sartel, D. L. Dheeraj, F. Jabeen, J. C. Harmand, *J. Cryst. Growth* **2010**, 312, 2073.
- [54] Mathworks documentation for 2-D correlation coefficient function corr2() for Matlab R2019b. <https://www.mathworks.com/help/images/ref/corr2.html?lang=en> (accessed: January 2020).